ORIGINAL PAPER

A multiscale framework for defining homeostasis in distal vascular trees: applications to the pulmonary circulation

Hamidreza Gharahi[1] · **Vasilina Filonova**[1] · **Haritha N. Mullagura**[2] · **Nitesh Nama**[3] · **Seungik Baek**[2] · **C. Alberto Figueroa**[1,4]

Abstract

Pulmonary arteries constitute a low-pressure network of vessels, often characterized as a bifurcating tree with heterogeneous vessel mechanics. Understanding the vascular complexity and establishing homeostasis is important to study diseases such as pulmonary arterial hypertension (PAH). The onset and early progression of PAH can be traced to changes in the morphometry and structure of the distal vasculature. Coupling hemodynamics with vessel wall growth and remodeling (G&R) is crucial for understanding pathology at distal vasculature. Accordingly, the goal of this study is to provide a multiscale modeling framework that embeds the essential features of arterial wall constituents coupled with the hemodynamics within an arterial network characterized by an extension of Murray's law. This framework will be used to establish the homeostatic baseline characteristics of a pulmonary arterial tree, including important parameters such as vessel radius, wall thickness and shear stress. To define the vascular homeostasis and hemodynamics in the tree, we consider two timescales: a cardiac cycle and a longer period of vascular adaptations. An iterative homeostatic optimization, which integrates a metabolic cost function minimization, the stress equilibrium, and hemodynamics, is performed at the slow timescale. In the fast timescale, the pulsatile blood flow dynamics is described by a Womersley's deformable wall analytical solution. Illustrative examples for symmetric and asymmetric trees are presented that provide baseline characteristics for the normal pulmonary arterial vasculature. The results are compared with diverse literature data on morphometry, structure, and mechanics of pulmonary arteries. The developed framework demonstrates a potential for advanced parametric studies and future G&R and hemodynamics modeling of PAH.

Keywords Homeostatic optimization · Growth and remodeling · Vasculature morphometry

Hamidreza Gharahi, Vasilina Filonova and Haritha N. Mullagura have contributed equally to this work.

✉ Hamidreza Gharahi
gharahih@med.umich.edu

[1] Section of Vascular Surgery, Department of Surgery, University of Michigan, Ann Arbor, MI, USA

[2] Department of Mechanical Engineering, Michigan State University, East Lansing, MI, USA

[3] Department of Mechanical & Materials Engineering, University of Nebraska-Lincoln, Lincoln, NE, USA

[4] Department of Biomedical Engineering, University of Michigan, Ann Arbor, MI, USA

1 Introduction

Pulmonary arterial tree is characterized by an intricate interplay between vessel wall structure, morphometry, and hemodynamics. Any anomaly such as pulmonary arterial hypertension (PAH) causes a significant deviation in the pathology from the homeostatic baseline condition, especially in the distal vasculature during the early progression of PAH. Briefly, the pathology of PAH effectively perturbs the pulmonary hemodynamics by altering the stiffness and resistance of the system (Hunter et al. 2008; Stacher et al. 2012). In turn, the altered hemodynamics upset the homeostatic balance in the vessel wall to modulate the disease progression (Truong et al. 2013; Tuder 2016). Therefore, a coupled study of the pulmonary arterial tree morphometry, hemodynamics, and vessel wall structure is essential to understand PAH or any other pulmonary vascular anomalies.

Computational frameworks that incorporate these components can significantly enhance our understanding of the mechanisms underlying in any of the disease progression in any of the distal pulmonary arterial tree.

A crucial component of such a computational framework is the identification of physiologically realistic tree morphometry since it defines the vascular resistance, and therefore significantly impacts hemodynamics. However, building physiologically realistic and complete morphometry of the distal pulmonary arterial tree is challenging due to limitations in data acquisition and modeling complexity (Burrowes et al. 2005). Due to the complexity of branching, pulmonary arteries of any given diameter can be distributed over a wide range of diameters (Clark and Tawhai 2018; Townsley 2012; Chambers et al. 2020; Marquis et al. 2021; Colebank et al. 2021). In his landmark study on design principles of vascular networks, Murray (1926) invoked the idea of minimum energy consumption by the biological systems to determine the bifurcation patterns (Murray's law). Specifically, he proposed that the diameter of a blood vessel is the result of a trade-off between the metabolic energy cost of maintaining blood volume in the vessel and the energy dissipated by viscous drag. Inspired by Murray's law, several approaches have been proposed to represent the architecture of vascular networks, including representation of the morphometry by fractal rules (Olufsen et al. 2000; Ionescu et al. 2009; Qureshi et al. 2014), or via a Strahler ordering technique to characterize the vessel connectivity (Jiang et al. 1994; Huang et al. 1996; Tamaddon et al. 2016).

Previous computational modeling efforts have extensively used vascular tree models to study the hemodynamics and fluid–solid-interactions (FSI) in multiscale arterial networks (Olufsen et al. 2000; Mittal et al. 2005; Huo and Kassab 2007; van de Vosse and Stergiopulos 2011; Qureshi et al. 2014). However, these studies have incorporated simplified representations of vessel wall that do not account for contributions of individual constituents of vessel wall such as elastin, collagen and smooth muscle cells, which is essential for study of structural changes associated with PAH. In addition, these studies focused on pulmonary hemodynamics over one cardiac cycle, thereby limiting their utility to study adaptations and disease progression. To truly understand the mechanical underpinnings of PAH, there is a need to develop computational models that allow long-term analysis of hemodynamics and FSI while integrating physiologically realistic tree morphometry and structurally motivated vessel wall models.

Another crucial component in understanding anomaly in pulmonary arteries is the study of the vessel wall structure and its changes over the course of any vascular disease, termed vascular growth and remodeling (G&R) (Ambrosi et al. 2011). A prominent biomechanical description of vascular G&R at a constitutive level is developed in the body

of work done by Humphrey and Rajagopal (2002) and Baek et al. (2007b). This approach employs a constrained mixture model (Humphrey and Rajagopal 2002) to describe the mechanical behavior of the vessel wall. The constrained mixture model integrates microstructural properties and cellular level functions of the vessel within a continuum mechanics framework, where the wall constituents are constrained to deform together but may have distinct mechanical properties and stresses. Thus, this model allows one to track the long-term (days to weeks) evolution of the vessel wall by incorporating constituent (elastin, collagen, and smooth muscle cells) mass fractions and their synthesis and removal as a function of biomechanical stimuli, such as stresses (wall shear stress and hoop stress). The G&R modeling framework suggests that in healthy condition, the blood vessel wall is maintained in a mechanical homeostatic state determined by cellular mechanotransduction. Accordingly, a key factor in the onset of G&R is a deviation of stresses from a homeostatic value, which is often determined by hemodynamics measurements on large vessels (pressure and flow). The homeostatic stresses, however, are not necessarily constant throughout an arterial network where hemodynamics significantly vary (Guo and Kassab 2004; Pries et al. 2005). Therefore, identifying the distal homeostatic characteristics of an arterial tree, morphometry, and hemodynamics is necessary in extending the G&R framework to arterial networks.

Finally, the coupling between the hemodynamics and G&R represents a temporal multiscale scenario in which the information must be transferred between a fast timescale (cardiac cycle in seconds) and slow timescale (synthesis and turnover of wall constitutions from days to months). This idea was first explored in the fluid–solid-growth (FSG) framework of (Figueroa et al. 2009), where the computational G&R model was coupled with hemodynamics (or FSI) for an individual vessel. The FSG framework proposed an iterative coupling between a slow-time G&R model of a single vessel with fast-time hemodynamics. Briefly, this approach assumed small deformations of the vessel wall over a cardiac cycle and linearized the material stiffness of the wall at the cycle-to-cycle averaged pressure in the intermediate configuration (Baek et al. 2007a). In turn, the hemodynamic forces (cycle-to-cycle averaged wall shear stresses and pressure) from FSI modeling were used as biomechanical stimuli for the G&R modeling. Following similar approach, a formal temporal multiscale approach for pulmonary arterial tree can be developed to couple the fast and slow timescales for computationally tractable FSG analysis.

The goal of this study is to develop a framework, namely homeostatic optimization, to identify the homeostatic characteristics of the distal pulmonary arterial tree. Our framework utilizes an extension of Murray's law proposed by Lindstrom et al. (2015). Briefly, we postulate that the homeostatic vessel geometry and composition are determined by

a minimization of energy dissipation under the constraint of mechanical equilibrium. Therefore, by formulating a constrained optimization problem in each vessel combined with morphometry, hemodynamics, and structural data from literature, we establish the homeostatic characteristics of a pulmonary arterial tree. The future goal of this work is to include growth and remodeling (G&R) of the pulmonary arterial tree by extending the temporal multiscale analysis of FSG. To this end, the hemodynamics of the arterial tree is described using Womersley's theory (1957) for fluid flow in deformable tubes, adapted to orthotropic materials and a bifurcating tree (Nichols et al. 2011; van de Vosse and Stergiopulos 2011). We must note that the focus of the current study is on the pulmonary arterial tree in homeostatic conditions which represents an instance of our slow timescale. Finally, we demonstrate our framework in three application examples: (1) A symmetric pulmonary tree with constant constituent mass fractions, (2) A symmetric pulmonary tree with variable constituent mass fractions, and (3) An asymmetric tree with variable constituent mass fractions.

2 Methods

2.1 Overview

In the beginning of this section, we describe the governing equations for the hemodynamics and fluid–solid interaction (FSI) in a 2D geometry of an arterial tree as shown in Fig. 1. We assume that the arterial network is symmetric in the radial direction, the equations are simplified and solved in 1D. First, we recognize two timescales: (1) A slow timescale to formulate the long-term vascular adaptations and homeostatic maintenance, and (2) A fast timescale to formulate the pulsatile nature of hemodynamics over a cardiac cycle. These two timescales are then coupled to formulate fluid–solid-growth (FSG) governing equations. The fluid solid interaction solution for one vessel is then extended for the entire geometry to solve for hemodynamics of the complete arterial network. The current framework is applied to a normotensive pulmonary arterial tree to study instantaneous hemodynamics. However, the formulation will hold for a future extension of FSG for long-term adaptations. In the

later part of this section, we estimate the baseline homeostatic optimization characteristics by using an extension of Murray's law for a single vessel. The energy optimization problem used for a single vessel homeostatic optimization estimation is generalized to the entire arterial network using an iterative process as described in Sect. 2.5. Finally, at the end of the methods section, we discuss the different model parameters introduced throughout the section with their estimated values.

2.2 Fluid–solid-growth governing equations

The mathematical description of the timescale separation is presented in Supplemental Materials A. Our timescale separation formulation provides a mathematical mean to justify the coupling between the fast and slow timescale analyses. The proposed formulation is analogous with the fluid–solid-growth FSG framework (Figueroa et al. 2009). However, a linear theory of fluid flow is used to model the hemodynamics.
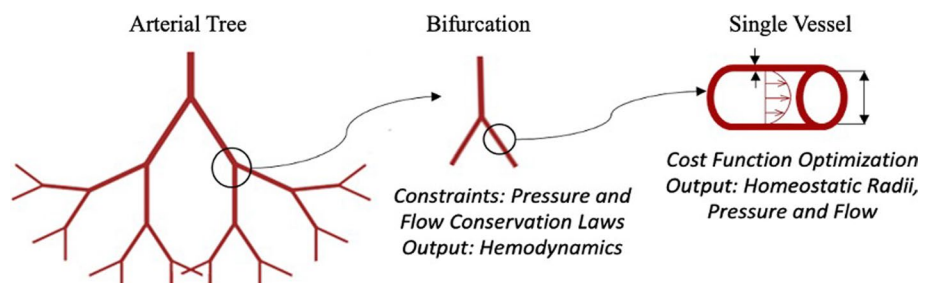
We begin our analysis by formulating the fast and slow time governing systems of equations. The two systems of equations are one-way coupled in time (from slow to fast) as the result of the proposed kinematics in (Supplemental Materials A). This one-way coupling of slow to fast systems of equations using the kinematics facilitates a system of governing equations that can be solved efficiently for multiscale study of arterial networks.

In our formulation, superscripts s and f correspond to slow and fast timescales, respectively. The slow time system describes fluid and solid equations governing the fluid velocity v^s, pressure p^s, and vessel wall displacements u^s, and the generalized 3D equations can be written as

$$\nabla_x \cdot v^s = 0, \ \nabla_x p^s = \mu \nabla_x^2 v^s, \\ 0 = \nabla_x \cdot P_{\text{solid}}^s(u^s) + b^s, \tag{1}$$

where μ is the constant viscosity of blood, P_{solid}^s is the averaged first Piola–Kirchhoff stress tensor, and b^s is an averaged body force vector. The fluid flow solution to the slow-time system of Eq. (1) in a 1D artery (Fig. 1) can be presented by Poiseuille law

Fig. 1 Schematic representation of the arterial tree, hemodynamic constraints at the bifurcation and the cost function optimization in a single vessel

Arterial Tree

Bifurcation

Constraints: Pressure and Flow Conservation Laws Output: Hemodynamics

Single Vessel

Cost Function Optimization Output: Homeostatic Radii, Pressure and Flow

$$q^s = \frac{\pi R^4 \Delta p^s}{8\mu L}, \tag{2}$$

where q^s is the steady-state flow rate, Δp^s is the steady-state pressure drop along the vessel, R is the vessel lumen radius, and L is the vessel length. The equilibrium equation for the vessel wall in (1) can be reduced to Laplace law for the cylindrical membrane, subjected to the distension pressure p^s (Supplemental Material B)

$$T_{\theta\theta}\big|_s = p^s R, \tag{3}$$

where wall tension $T_{\theta\theta}\big|_s$ is computed by a constrained mixture model of the vessel.

The fast time system describes fluid and solid equations that define the fast time fluid velocity v^f, pressure p^f, and displacements u^f which oscillate around at a given slow time state. The generalized 3D governing system of equations can be expressed as

$$\nabla_x \cdot v^f = 0, \quad \rho_{\text{fluid}} \frac{\partial v^f}{\partial t}\bigg|_x = -\nabla_x p^f + \mu \nabla_x^2 v^f,$$
$$\rho_{\text{solid}} \frac{\partial^2 u^f}{\partial t^2}\bigg|_x = \nabla_x \cdot P^f_{\text{solid}}\big|_s + b^f, \tag{4}$$

where ρ_{fluid} and ρ_{solid} are the blood and wall density, respectively. The first Piola–Kirchhoff $P^f_{\text{solid}}\big|_s$ is defined as a linearization of the constrained mixture model at a given slow time state s, and b^f is the body force vector. The solution to the fast-time system of Eq. (4) in an artery can be described by Womersley's theory of the oscillatory flow in deformable tubes (Womersley 1957). This theory provides an analytical solution (Filonova et al. 2020) for the fast-time periodic variables at a given frequency ω

$$p^f = P e^{i\omega\left(t-\frac{z}{c}\right)}, q^f = Q e^{i\omega\left(t-\frac{z}{c}\right)}, Q = \frac{\pi R^2 P}{c\rho_{\text{fluid}}}(1-g),$$
$$v_z^f = \frac{P}{c\rho_{\text{fluid}}}(1-j)e^{i\omega\left(t-\frac{z}{c}\right)} \tag{5}$$

where q^f is the fast-time flow rate, v_z^f is the fast-time longitudinal velocity, and P and Q are fast-time pressure and flow in the frequency domain, z is a coordinate along the longitudinal axis of the vessel. The solution is expressed via Bessel functions of the first kind J_0, J_1, $g = 2J_1(\bigwedge)/\bigwedge J_0(\bigwedge)$, $j = J_0\left(\frac{\bigwedge r}{R}\right)/\bigwedge J_0(\bigwedge)$, and $\bigwedge = i^{3/2}\alpha_{\text{Wom}}$ with the Womersley number defined as $\alpha_{\text{Wom}} = R\sqrt{\omega\rho_{\text{fluid}}/\mu}$.

In the current study we consider the orthotropic membrane stiffness, and therefore, accordingly the pulse wave velocity relation from Womersley's solution has been accordingly modified.

Pulse wave velocity is an important clinical factor in monitoring the systemic and pulmonary hypertension. The pulse wave velocity c can be computed using Womersley's solution.

$$c = \sqrt{\frac{(1-g)h \mathcal{A}_{\theta\theta}\big|_s}{2R\rho_{\text{fluid}}}}. \tag{6}$$

The total pressure p and flow rate q in the time domain are obtained by applying Fourier series to the solutions (5) for multiple frequencies $\omega_n = 2\pi n/T$ superimposed by the slow-time solution (2) and (3) at zero frequency

$$p = p^s + \sum_{n=1}^{\infty} P_n e^{i\omega_n(t-z/c_n)}, q = q^s + \sum_{n=1}^{\infty} Q_n e^{i\omega_n(t-z/c_n)}, \tag{7}$$

where P_n and Q_n are frequency dependent coefficients of oscillatory fields. Once the pressure and flow are known, we can compute the hydraulic resistance *Res* and characteristic impedance of the vessel $Z^c(\omega)$ using the relations from Eqs. (2), (5) and (6).

$$Z^c(\omega) = \frac{P}{Q} = \frac{c\rho_{\text{fluid}}}{\pi R^2(1-g)} = \frac{1}{\pi R^2}\sqrt{\frac{h\rho_{\text{fluid}} \mathcal{A}_{\theta\theta}\big|_{p^s}}{2R(1-g)}},$$
$$\text{Res} = \frac{\Delta p^s}{q^s} = \frac{8\mu L}{\pi R^4}, \tag{8}$$

where $\mathcal{A}_{\theta\theta}\big|_s$ is the circumferential component of the stiffness tensor for a vessel (Supplemental Materials A & H) (Filonova et al. 2020). We must note that the characteristic impedance in the time domain is $z^c = p^s(0)/q^s + \text{Res} + \sum_{n=1}^{\infty} Z_n^c e^{iw_n t}$. Similarly, we can compute the input impedance $Z^{\text{inp}}(\omega) = P/Q\big|_{z=0}$ and terminal impedance $Z^T(\omega) = P/Q\big|_{z=L}$ of the vessel.

2.3 Hemodynamics in an arterial tree

The fluid–solid interaction solution of one vessel is extended to an entire arterial tree. We consider the pulmonary arterial network as a 1D bifurcating tree (as shown in Fig. 1), where each vessel can be characterized by a radius and length. Following the previous section, the total hemodynamics is the summation of the slow-time and fast-time hemodynamics. The slow-time hemodynamics in the arterial tree is computed using Poiseuille flow for each vessel, the flow conservation and pressure continuity for each bifurcation, and boundary conditions at the tree inlet and outlets (Supplemental Materials C). Given the arterial tree morphometry and linearized vessel wall stiffnesses, we can compute the fast-time hemodynamics using Womersley's solution.

First, at each bifurcation of the arterial tree we decompose the fast-time pressure and flow to forward and backward (reflection) waves

$$P = P_{\text{forw}} + P_{\text{back}}, \quad P_{\text{forw}} = H_{\text{forw}} e^{-i\omega z/c}, \quad P_{\text{back}} = H_{\text{back}} e^{i\omega z/c}$$

$$Q = Q_{\text{forw}} + Q_{\text{back}}, \quad Q_{\text{forw}} = \frac{H_{\text{forw}}}{Z^c} e^{-i\omega z/c}, \quad Q_{\text{back}} = -\frac{H_{\text{back}}}{Z^c} e^{i\omega z/c}$$

$$(9)$$

with constant coefficients H_{forw} and H_{back} for individual harmonics. The characteristic impedance Z^c and pulse wave velocity c are the same for both forward and backward waves (van de Vosse and Stergiopulos 2011). Therefore, we define the reflection coefficient Γ at the end of an individual vessel as (Taylor 1957; Avolio 1980)

$$\Gamma = \frac{Z^T - Z^c}{Z^T + Z^c} = \left. \frac{P_{\text{back}}}{P_{\text{forw}}} \right|_{z=L}. \tag{10}$$

$$\Gamma = \frac{H_{\text{back}}}{H_{\text{forw}}} e^{\frac{i\omega 2L}{c}}$$

The reflection coefficient Γ varies between -1 and 1 with $\Gamma = 0$ indicating no wave reflection in the vessel, i.e., matching impedance $Z^T = Z^c$. Specifically, $\Gamma = -1$ and $\Gamma = 1$ represent open-end type (or negative) and closed-end type (or positive) wave reflections, respectively. Next, the impedance along each vessel can be expressed as

$$Z(z, \omega) = \frac{P}{Q}(z, \omega) = \frac{P_{\text{forw}} + P_{\text{back}}}{Q_{\text{forw}} + Q_{\text{back}}} = Z^c \frac{1 + \Gamma e^{\frac{i\omega 2(z-L)}{c}}}{1 - \Gamma e^{\frac{i\omega 2(z-L)}{c}}} \tag{11}$$

In addition, the oscillatory pressure and flow along the vessel using (9) and (10) can be written as

$$P(z, \omega) = H_{\text{forw}} e^{-i\omega z/c} (1 + \Gamma e^{i\omega 2(z-L)/c}), \quad Q(z, \omega)$$
$$= \frac{H_{\text{forw}}}{Z^c} e^{-i\omega z/c} (1 - \Gamma e^{i\omega 2(z-L)/c}). \tag{12}$$

Each bifurcation is characterized by a parent vessel and two daughter vessels. Considering the conservation of flow and pressure continuity at each bifurcation, we obtain the terminal impedance ($z = L$) in the parent vessel

$$Z_p^T = \left(\frac{1}{Z_{d1}^{\text{inp}}} + \frac{1}{Z_{d2}^{\text{inp}}} \right)^{-1}, \tag{13}$$

where the input impedance for each daughter vessel is computed from (11) by setting $z = 0$

$$Z^{\text{inp}} = Z^c \frac{1 + \Gamma e^{-i\omega 2L/c}}{1 - \Gamma e^{-i\omega 2L/c}}. \tag{14}$$

Given the flow at the root vessel and the terminal pressure and reflection coefficient at the outlets, we use the bifurcation relation (13) to compute the input impedance (14) and reflection coefficient (10) from bottom-to-top. Finally, we can reconstruct the pressure and flow at each vessel of the tree from top-to-bottom, using (12). The

algorithmic details of the solution are given in Supplemental Materials D.

2.4 Homeostatic optimization

In this section, we describe a method to estimate the homeostatic baseline characteristics of an entire arterial tree (as shown in Fig. 1) based on an extension of Murray's law that integrates the mechanics of vessels. The proposed optimization is an energy-based minimization problem that integrates morphometry, hemodynamics, and individual vessel mechanics essentially operates at the slow timescale. Therefore, the optimization constraints include the slow-time hemodynamics solution and Laplace law (Sect. 2.2). In this work, the morphometry of the tree is described by the generation number, where the most proximal vessels is considered generation 1, and each bifurcation increments the generation number by 1. Upon solving the energy minimization problem, the homeostatic radii distribution over the pulmonary arterial tree can be determined for each generation of the arterial tree.

Following the study by Lindström et al. (2015), we assume that the blood vessel wall composition and geometry strive to optimize the energy consumption. This energy consumption includes the metabolic demand for maintaining the volume of the blood in a vessel and the power needed to overcome hydraulic resistance. In addition, we must account for the metabolic demand for the maintenance (synthesis and removal) of vessel wall constituents. We assume that the homeostatic state is governed by such an optimization rule that can be defined for each individual vessel.

The formulation of the optimization problem is as follows. First, the metabolic power needed for blood supply is proportional to the blood volume that needs to be sustained, with a factor ϑ^{blood}. This metabolic power per unit length can be written as $C_{\text{blood}} = \vartheta^{\text{blood}} \pi R^2$, and R is the vessel radius in homeostatic conditions. Second, the power per unit length needed to overcome the resistance of Poiseuille flow (viscous drag forces) is $C_{\text{drag}} = 8\mu q^{s2}/(\rho_{\text{fluid}} \pi R^4)$. Third, the metabolic energy cost is assumed to be proportional to the mass of each vessel wall constituent $C_{\text{wall}} = (\frac{2\pi R}{\rho_{\text{solid}}}) \sum_i \vartheta^i M_R^i$, where M_R^i is the mass per unit reference area of each constituent with $i \in \{\text{el, smc, col}\}$ representing elastin, smooth muscle cells (SMCs), and collagen fibers, respectively. The constants ϑ^i are the metabolic energy cost of the vessel wall constituents. The metabolic cost of smooth muscle cells (SMC) ϑ^{smc} includes the metabolic cost of maintenance $\vartheta^{\text{smc}}_{\text{maint}}$ and active tension $\vartheta^{\text{smc}}_{\text{act}}$ (Lindström et al. 2015). Collectively, the total energy cost per unit length for an individual blood vessel can be written as

$$C\left(M_R^i, R; q^s\right) = C_{\text{blood}} + C_{\text{drag}} + C_{\text{wall}}$$

$$= \vartheta^{\text{blood}} \pi R^2 + \frac{8\mu q^{s2}}{\rho_{\text{fluid}} R^4} + \frac{2\pi R}{\rho_{\text{solid}}} \sum_i \vartheta^i M_R^i. \qquad (15)$$

The energy cost function in (15) has to be minimized with the mechanical equilibrium, represented by Laplace law, as a constraint. First, we rewrite Laplace law in terms of the mass of vessel wall constituents. Accordingly, we define the total mass as M_R^{total} and mass fractions of elastin, SMCs, and collagen fibers as $v^{\text{el}} = M_R^{\text{el}} / M_R^{\text{total}}$, $v^{\text{smc}} = M_R^{\text{smc}} / M_R^{\text{total}}$, and $v^{\text{col}} = \sum_k v^k$, respectively, with k-th collagen-fiber-family mass fraction $v^k = M_R^k / M_R^{\text{total}}$. The circumferential membrane stress $T_{\theta\theta}$ can be written as (Supplemental Materials B):

$$T_{\theta\theta} = \frac{M_R^{\text{total}}}{(1 - \phi_f)\rho_{\text{solid}}\lambda_\theta \lambda_z} \sum_i v^i \sigma_\theta^i, \qquad (16)$$

where the parameter ϕ_f is the volume fraction of the interstitial fluid, usually taken as 0.7. The λ_θ and λ_z are the circumferential and axial stretches, respectively, which correspond to stretches mapping from a reference configuration to the current configuration (Supplemental Materials B). The circumferentially acting σ_θ^i part of the Cauchy stress tensor $\boldsymbol{\sigma}^i$ is defined as

$$\sigma^i = \frac{1}{h^i}\mathbf{T}^i, \quad h^i = \frac{M_R^i}{(1 - \phi_f)\rho_{\text{solid}}\lambda_\theta \lambda_z}, \qquad (17)$$

where h^i is the effective thickness of each constituent in the vessel wall. We must note that the total thickness of the arteries h is defined as the sum of the constituent-wise thicknesses. Variations in hemodynamics under physiological conditions change the vessel wall stresses which leads to adaptive responses from the vascular wall cells (endothelial cells, SMCs, and fibroblasts). In the homeostatic state, however, the stress of each constituent σ_θ^i is determined by the stretch at which the constituents are deposited, namely prestretches. Accordingly, we assume that the reference configuration in our model is the homeostatic configuration. Therefore, to evaluate vascular tension in the homeostatic condition we must set $\lambda_\theta = \lambda_z = 1$. Substituting (16) to Laplace law (3), we obtain the constraint

$$\overline{p}^s R = \frac{M_R^{\text{total}}}{(1 - \phi_f)\rho_{\text{solid}}} \sum_i v^i \sigma_\theta^i \qquad (18)$$

The pressure p^s in a single vessel is not constant, therefore $\overline{p}^s$ is the mid-vessel pressure which is the mean of the inlet and terminal pressure of a single vessel. On the other hand, flow q^s in a single vessel is constant which is the same as the mean blood flow in the vessel. Finally, embedding the constraint into the metabolic cost function

for a single vessel (15), we can rewrite the optimization problem in terms of R

$$C\left(R; \overline{p}^s, q^s\right) = \vartheta^{\text{blood}} \pi R^2$$

$$+ \frac{8\mu q^{s2}}{\rho_{\text{fluid}} \pi R^4} + 2\pi\left(1 - \phi_f\right)\overline{p}^s R^2 \frac{\sum_i \vartheta^i v^i}{\sum_i v^i \sigma_\theta^i} \qquad (19)$$

Minimization of this cost function with respect to radius governs the homeostatic state of a single vessel whose mean pressure and flow are known (Supplemental Materials E). This optimization is generalized to an entire arterial tree as described in the next section.

2.5 Iterative process of optimization

To generalize the homeostatic optimization to an arterial tree, a global hemodynamic constraint must be considered to determine $\overline{p}^s$ and q^s for each vessel. This hemodynamic constraint is coupled with the optimization problem in an iterative manner. To implement this iterative algorithm (Supplementary Materials E), we first construct a tree with vessel connectivity from the literature (based on a fractal rule or Strahler ordering) and initial guesses for diameters. Second, using this tree structure, the slow-time hemodynamics problem is solved for the entire tree (Supplementary Materials E). The boundary conditions for the hemodynamic problem are either pressure or flow, imposed at the inlet and outlets of the tree. Third, to update the vessel radii, the cost function minimization problem is solved in each segment using Newton–Raphson method (Supplementary Materials G). The second and third steps are repeated until convergence is achieved, i.e., the hemodynamics remain constant across two subsequent iterations. Figure 2 shows the schematic of the implementation.

We must note that in the current framework the fast-time hemodynamics in a tree is solved after the homeostatic characteristics are established. This one-way coupling (slow time to fast time) is facilitated through computing the stiffness $\mathcal{A}_{\theta\theta}|_s$, by linearization of the constrained mixture model of each vessel. In accordance with this coupling, we present the homeostatic optimization results (vessel radii upon minimization of Eq. (19) followed by the results for the pulsatile hemodynamics for each example).

2.6 Model parameters

To illustrate our framework, we apply our model to estimate the homeostatic characteristics and hemodynamics of the intermediate and small pulmonary arteries (with radius of 0.5–0.01 cm). The arterial network considered in our framework starts from the fourth distal vessel (first being the main pulmonary artery) for up to the next nineteen generations.

Fig. 2 Schematic representation of the iterative process for homeostatic optimization: vessel stiffness, length, radius, wall composition and thickness are defined for individual vessels and the metabolic cost function is used to iteratively optimize for the radii using slow-time hemodynamics in the entire tree
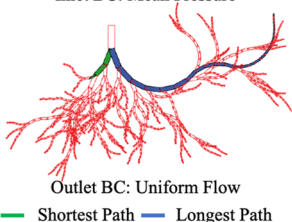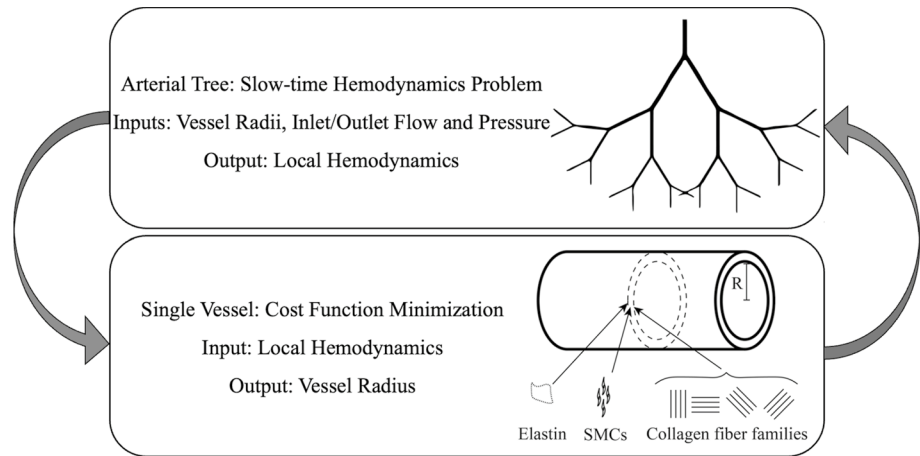

We illustrate our framework in three examples as shown in Table 1: (1) A symmetric pulmonary tree with constant constituent mass fractions (Case 1), (2) A symmetric pulmonary tree with variable constituent mass fractions (Case 2), and (3) An asymmetric tree with variable constituent mass fractions (Case 3).

For the pulsatile hemodynamics, we prescribe an input flow waveform taken from normotensive human measurements in the main pulmonary artery (Zambrano et al. 2018) scaled to fourth distal vessel (first being the main pulmonary artery) downstream assuming an even split at initial three bifurcations. In addition, the first nine harmonics are used to represent pressure and flow waveforms in the frequency domain. Furthermore, a terminal reflection coefficient is prescribed at the terminal vessels for fast-time hemodynamics. For the symmetric tree applications of the homeostatic optimization, as shown in Table 1, we prescribe at the inlet the mean flow, and at the outlets a terminal pressure (assumed to be close to the capillary pressure). In the asymmetric tree, however, we prescribe the inlet mean pressure (12 mmHg)

and uniform flow at the outlets (mean flow/number of outlets). In all examples, $L(R)$ can be described using the relation given in (Olufsen et al. 2012) which approximates the human morphometric data from a single pulmonary arterial tree cast (Huang et al. 1996). We modified $L(R)$, scaling it by factor of half, to obtain the lengths closer to observations in the proximal vessels from the literature data (as shown in Fig. 4).

Elastin in human arteries is mostly produced in early ages, and due to a long half-life, its content remains relatively constant over time in normal conditions. Therefore, in this study the metabolic energy cost of elastin is neglected, $\vartheta^{el} = 0$. The metabolic cost coefficients ϑ^i of maintenance of SMCs and collagen in the normotensive vessel wall are estimated to be the order of 1000 W/m^3 (Liu and Kassab 2007). Although the metabolic cost of these constituents may vary throughout the arterial tree, we chose the value 1500 W/m^3 for the entire tree, as shown in Table 2. The metabolic cost of active tension in SMCs was experimentally measured and reported in (Paul 1980).

Table 1 Summary of the three cases of the arterial tree framework

Parameter	Case 1	Case 2	Case 3
Geometry	Symmetric Arterial Tree Inlet BC: Mean Flow Outlet BC: Terminal Pressure	Symmetric Arterial Tree Inlet BC: Mean Flow Outlet BC: Terminal Pressure	Asymmetric Arterial Tree Inlet BC: Mean Pressure Outlet BC: Uniform Flow — Shortest Path — Longest Path
Mass Fraction of the Wall Constituents (Elastin, Smooth Muscle Cells and Collagen)	Constant across the Arterial Tree	Varies across the Arterial Tree	Varies across the Arterial Tree

Based on this study, Taber (1998) determined the value of active tension metabolic cost to be 0.00872 W/N.m and proportional to the active tension. Since the active tension is proportional to the content of SMCs in the vessel wall, the metabolic cost can be assumed to be proportional to SMC content (Supplementary Materials D). Furthermore, the metabolic energy requirements for maintaining blood in arteries are adopted from Liu et al. (2012) based on the number of red blood cells, white blood cells, and platelets in a unit volume of blood and their corresponding oxygen consumption rate for a normal adult human subject.

A constrained mixture model (Seyedsalehi et al. 2015) is used to simulate the mechanics of vessels (Supplementary Materials B). The passive mechanical properties of the proximal vessels are calibrated against experimental data from inflation tests on pulmonary arteries of pigs (Wang et al. 2020). In the current study, we assume that the individual constituents preserve their mechanical behavior in different locations along the tree, and the deposition stretches vary depending on their local transmural pressure. Therefore, intrinsic mechanical parameters wall constituents are considered constant (i.e., constant passive stiffnesses ($c_1 - c_5$) and active properties S, λ_0, and λ_M), whereas the prestretches ($G_\theta^{el}, G_z^{el}, G_h^{col}$, and G_h^{smc}) are

calibrated in each vessel by matching the experimental thickness-to-diameter ratio (~ 7% to 16% from large arteries to microvessels) reported in (Li et al. 2012; Rol et al. 2017).

In Case 1, constant mass fractions for the constituents are prescribed in the entire arterial tree. The adventitial layer of the arterial wall was assumed to be comprised of 95% of collagen and 5% of elastin. Furthermore, Mackay and colleagues (Mackay et al. 1978) reported the mass fractions of the constituents in the medial layer of pulmonary arteries in healthy humans. The mass fractions, therefore, are estimated using the relative layer-wise thicknesses reported in (Chazova et al. 1995). However, the pulmonary arterial wall composition varies throughout the arterial tree (Elliott and Reid 1965). The variable composition of the vessel wall is reflected in Cases 2 & 3 by varying the content of elastin and SMCs in the medial layer using data from (Chazova et al. 1995) (Fig. 3). Particularly, most of the arteries larger than 0.32 cm in diameter are elastic arteries endowed with multiple layers of elastic lamina. As arteries become smaller, their structure transitions from elastic to muscular type over a range of 0.32–0.2 cm where the elastic layers fragment and are replaced by SMC (Elliott and Reid 1965). The arteries smaller than 0.2 cm have a muscular media with two

Table 2 Model parameters for homeostatic optimization and pulsatile hemodynamics

Parameter description		Reference
Extended Murray's law		
Metabolic cost of collagen and SMCs $\vartheta^{col}, \vartheta^{smc}_{maint}$	1500 W/m³	(Liu and Kassab 2007)
Metabolic cost of elastin ϑ^{el}	0 W/m³	
Metabolic cost of blood supply ϑ^{blood}	51.7 W/m³	(Liu et al. 2012)
Metabolic cost of active tension ϑ^{smc}_{act}	0.00872 s⁻¹	(Paul 1980)
Vessel wall mechanical properties		
Wall density ρ_{solid}	1060 kg/m³	
Constant mass fractions v^{el}, v^{smc}, v^{col}	77% collagen, 12% SMCs, 11% elastin	(Mackay et al. 1978) (Chazova et al. 1995)
Variable mass fractions v^{el}, v^{smc}, v^{col}	Shown in Fig. 3	(Elliott and Reid 1965)
Constrained mixture model parameters (Supplemental Materials B)	$c_1 = 28.83, c_2 = 178.59, c_4 = 24.51$N.m/kg $c_3 = 1.05, c_5 = 0.75$ $\alpha^c = 0, \pm 45, 90$ $\lambda_M = 1.2, \lambda_0 = 0.7$ $S = 20$kPa	Fit to data in (Wang et al. 2020)
Hemodynamics		
Input flow waveform, scaled by 1/8	mean flow 11.65 ml/s	(Zambrano et al. 2018)
Length-to-radius relation $L(R)$	$L = 6.2 R^{1.1}$ mm	
Mean terminal pressure (Cases 1 & 2) p_T^s	10 mmHg	(Qureshi et al. 2014)
Terminal reflection coefficient Γ	− 1	(Hollander et al. 2001)
Blood density ρ_{fluid}	1060 kg/m³	
Dynamic viscosity μ	0.0035 Pa sec	

distinctive internal and external elastic laminas (Hislop and Reid 1978). Although arteries smaller than 0.01 cm are not included in this study, we must note that the number of muscular arteries significantly drops when an arterial size approaches 0.01 cm and below. In this region, the vessels become partially or non-muscular.

3 Results

In this section the morphometric, hemodynamics and homeostatic optimization results are presented for the three different cases of the arterial tree framework (Table 1) and are compared to published data.

3.1 Case 1: Symmetric tree with constant mass fractions

Figure 4 shows the results of the morphometric and hemodynamics results of the homeostatic optimization. Figure 4a shows vessel diameters resulting from the homeostatic optimization. The morphometry study (Huang et al. 1996) reported 15 orders of arteries in a human lung using the Strahler ordering system, where the first and fifteenth order vessels correspond to precapillary vessels and right/left pulmonary arteries, respectively. A comparison of our results with data from this study indicates an agreement between our first generation and their fourteenth order vessels which are located at two bifurcations downstream to the pulmonary trunk. The vessel lengths are depicted in Fig. 4b and compared to human data on proximal pulmonary arteries. In addition, the exponent ξ in the daughter-to-parent radius relation $D_p^\xi = D_{d1}^\xi + D_{pd2}^\xi$ is determined to be approximately cubic (2.980 ± 0.004) along the tree (consistent with the original Murray's law). The daughter-to-parent area ratio a_d/a_p is almost constant and falls in the range of 1.2–1.3. The thickness-to-diameter ratio is shown in Fig. 4c, comparing a range of values reported in experimental studies (Li et al. 2012; Rol et al. 2017). This ratio increases distally which is consistent with a trend observed in arterial networks in the systemic circulation (Guo and Kassab 2004; Pries et al. 2005). Pressure distribution along the tree is shown in Fig. 4d. The pressure gradient becomes steeper toward the terminal vessels where most of the pulmonary arterial resistance resides.

Figure 5a shows the axial E_{ZZ} and circumferential $E_{\theta\theta}$ Young's moduli, linearized at the estimated luminal pressure, and structural stiffness of pulmonary vessels across the symmetric tree. The axial Young's moduli are markedly lower than those in the circumferential direction (Baek et al. 2007a; Bernal et al. 2011) and both are decreasing across the generations. Figure 5b shows a

comparison of the structural stiffness $E_{\theta\theta}h/R_0$ as a result of the homeostatic optimization, with data in (Krenz and Dawson 2003; Yen et al. 1990; Wang et al. 2020). Of note, the experiments in (Wang et al. 2020) were conducted only on the main porcine pulmonary vessels, and the value for the first generation is presented in Fig. 5b for the comparison purpose.

Next, we demonstrate the results of the fast-time hemodynamic analysis. The most valuable outcome from modeling for the pulsatile flow in the distal vasculature is an estimation of the pulse wave velocity across the tree (Fig. 6a). The pulse wave velocity c depends on the wall stiffness as well as Womersley's number α_{Wom} in (8), which is shown for the first and the ninth harmonics (Fig. 6b). Thus, the steep decrease of the pulse wave velocity across the generations is the result of vessel dimension variability, decrease in α_{Wom}, and heterogeneity of wall stiffness (Fig. 5b). The idealized Moens–Korteweg pulse wave velocity c^{MK} is plotted for the comparison. The pulse wave velocity as a result of the homeostatic optimization agrees with the experimental data measured for large human pulmonary arteries marked on the first generation (Milnor et al. 1969; Banks et al. 1978).

3.2 Case 2: symmetric tree with variable mass fractions

Figure 7 shows the homeostatic optimization results of the Case 2 compared to Case 1. The sudden variation in the radial exponent ξ between third and sixth generations corresponds to the transition region of the vessel from elastic to muscular arteries (Fig. 7a). Homeostatic values of the mechanical stresses are plotted in Fig. 7b and d. The wall shear stress value τ is within 1–2.5 Pa for Case 1 that was observed in the systemic circulation (Kamiya et al. 1984; Pries et al. 1995). Similar wall shear stress is observed in Case 2, which follows an increasing trend across the tree ranging from 1.14 to 1.27 Pa from larger to smaller vessels (Fig. 7b). Figure 7c shows a step-drop in longitudinal Young's modulus as blood vessels become more muscular in Case 2 as opposed to the linear trend in Case 1. The decreasing trend of hoop stress in Case 1 (Fig. 7d) is also compatible with observations in the systemic circulation (Guo and Kassab 2004; Pries and Secomb 2005), although the values are significantly smaller. On the other hand, Case 2 has a slight increase in the stiffness measure Eh/R_0 leading to an increased average and a reduced variability along the tree (Fig. 7d).

3.3 Case 3: asymmetric tree with variable mass fractions

Finally, we apply our framework to an illustrative reconstruction of a pulmonary arterial tree based on vessel connectivity
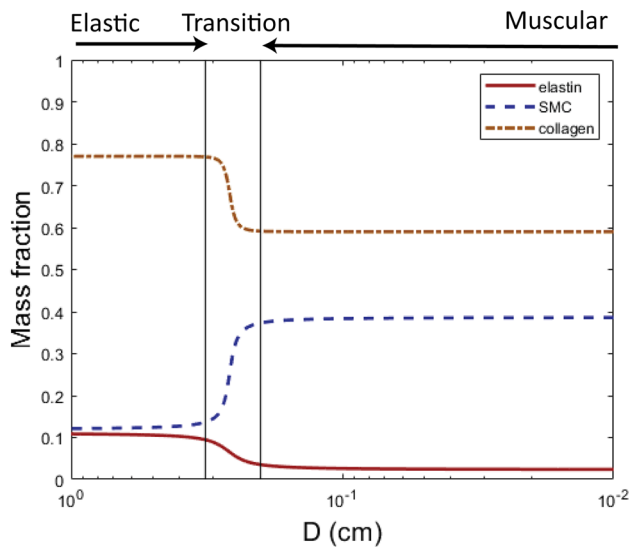
Fig. 3 Prescribed variable mass fractions of the wall constituents: elastin, smooth muscle cells and collagen. The arrows on the top show the trend in arterial composition

data on the first five largest orders of vessels in Huang et al. (1996) (see details of tree reconstruction and initialization in Supplemental materials G). In this example, we use the mass fraction values from Case 2. However, the pressure is prescribed at the inlet and uniform flow is prescribed at outlets as boundary conditions. The input pressure is taken

from the symmetric tree results as 11.92 mmHg. Flow at outlets is prescribed by assuming an even split of input flow, 11.65 ml/s, among all outlets. To illustrate the results, we use the cumulative distance of middle of each arterial segment from the root of the arterial tree X. Figure 8 depicts the results of our optimization on this tree. Figure 8a shows a schematic of our asymmetric tree, where the shortest path and the longest paths along the pulmonary arterial tree are highlighted. The shortest path includes five generations, whereas the longest path includes 28 generations of vessels. Slow time pressure is illustrated for all the vessels in Fig. 8b. Clearly, the shortest and longest path results bound the distributions. Furthermore, the stratification of pressure along the generations shows a low variability of pressure within each generation. The stiffness measure and wall shear stress follow the same trends as Case 2 of the symmetric example. However, the stiffness measure is distributed around 9 kPa and falls below the experimental observations (Fig. 8c).

Next, we simulate the pulsatile hemodynamics in the asymmetric tree. Figure 9 shows the pulse wave velocity for the shortest and longest paths across the pulmonary arterial tree. Similar to the symmetric tree cases, the pulse wave velocity is close to measurements in main pulmonary arteries reported in (Milnor et al. 1969; Banks et al. 1978).

Figure 10 shows the pulsatile hemodynamics solution along the symmetric and asymmetric vascular tree. In case of symmetric tree (Fig. 10a), the total input flow splits evenly at each generation. The total terminal pressure is

Fig. 4 Symmetric tree—homeostatic optimization results plotted against generation number: **a** diameter distribution compared to reported data of large vessels; **b** length distribution compared to reported data of large vessels. Structural and hemodynamics results plotted against vessel diameter: **c** wall thickness-to-diameter ratio compared to reported data; **d** mid-vessel pressure
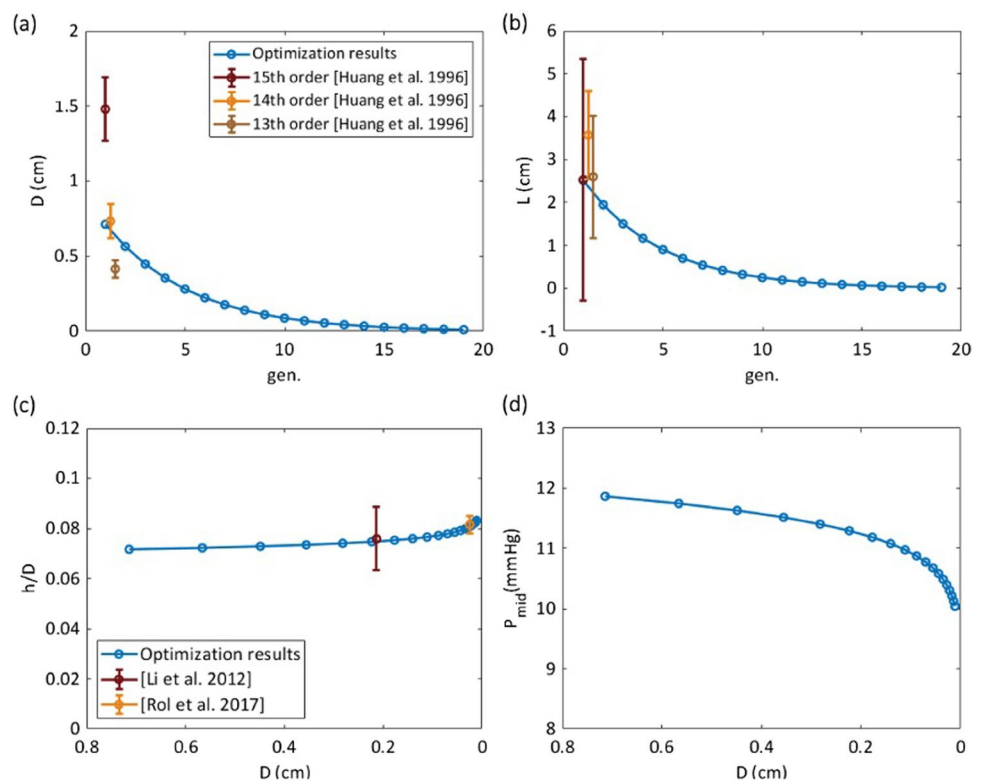
within the physiological range 8–25 mmHg. The minimum diastolic pressure falls below the mean pressure in proximal vessels that can be explained by negative type of wave reflection. Note that using Eq. (10), we obtain negative values of the reflection coefficient's real part at the end of each vessel in the range of (-1, -0.32). In asymmetric tree, pulsatile hemodynamics is plotted for the longest and shortest paths in Fig. 10b, c. The total input flow splits at every bifurcation, giving a greater fraction of flow to the longest path. Moreover, the backflow is more significant in the asymmetric case compared to the symmetric cases. Similar to Case 1, however, the total terminal pressure clearly has negative wave reflections.

4 Discussion

Experimental studies have recognized the multiscale nature of pulmonary arterial tree in structure and function, and emphasized the importance of vascular remodeling. At the structural level, pulmonary vascular remodeling associated with PAH involves increased collagen deposition, degradation of elastin, and SMC proliferation, which culminate in stiffening and thickening of the vessel wall (Wang and Chesler 2011). At the vascular tree level, morphometric changes such as rarefaction have been observed in PAH

(Humbert et al. 2019). Hemodynamic factors (mean/pulse pressure, wall shear stress, etc.) in the cardiopulmonary system significantly contribute to onset and progression of these pathologies. Previous studies on vascular G&R have postulated that the vascular G&R is indeed caused by a departure from the homeostatic baseline (Humphrey et al. 2014). Taken together, the study of G&R in PAH necessitates an integrated study of the pulmonary arterial tree morphometry, hemodynamics, and vessel wall structure.

Figueroa et al. (2009) introduced the fluid–solid-growth FSG framework to study the coupling between the hemodynamics and G&R. Motivated by the FSG framework, we outlined the key ideas for developing a temporal multiscale framework to study long-term adaptations in PAH. We then generalized Womersley's linear theory to model the fluid–solid-interactions in an arterial tree. Furthermore, we developed a novel method for establishing the homeostatic baseline for a pulmonary arterial network using metabolic energy considerations. Based on an extended Murray's law, we assumed that the equilibrium state of an arterial network minimizes the total metabolic energy consumption. Therefore, a cost function was formulated to incorporate the metabolic needs for blood supply in a vessel and for maintenance of the vessel wall constituents, and energy dissipation due to blood viscosity. The optimization of this cost function resulted in the vessel radii, content of constituents, and

Fig. 5 Symmetric tree—homeostatic optimization results for the wall stiffness versus generation number: **a** Young's modules in circumferential and longitudinal directions; **b** stiffness measure—circumferential structural stiffness divided by unstressed radius and compared to distensibility relations from data
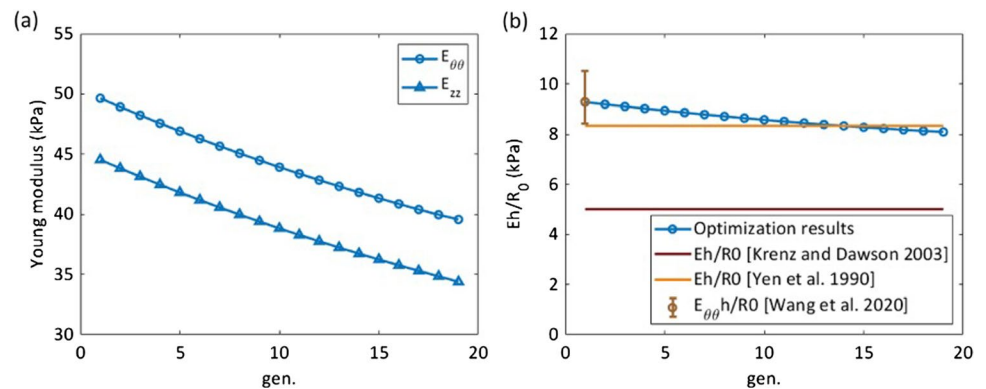
Fig. 6 Symmetric tree—pulsatile hemodynamics results versus generation number: **a** pulse wave velocity for two harmonics, compared to data and Moens–Korteweg speed values; **b** Womersley's number for two harmonics
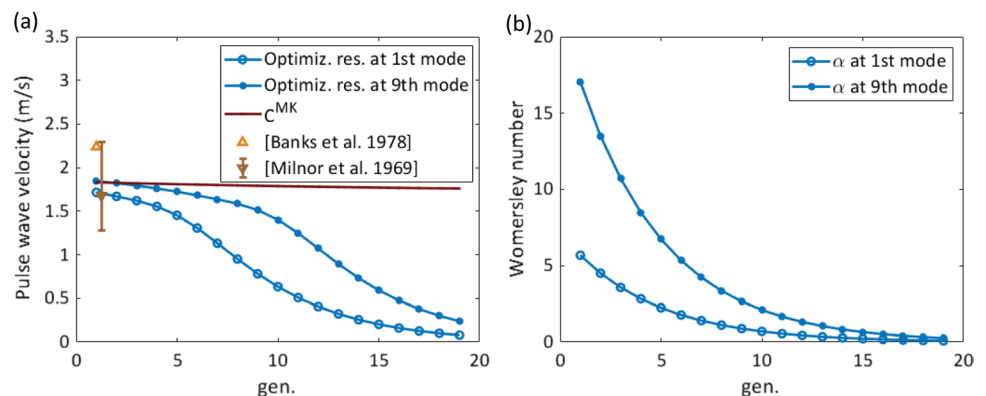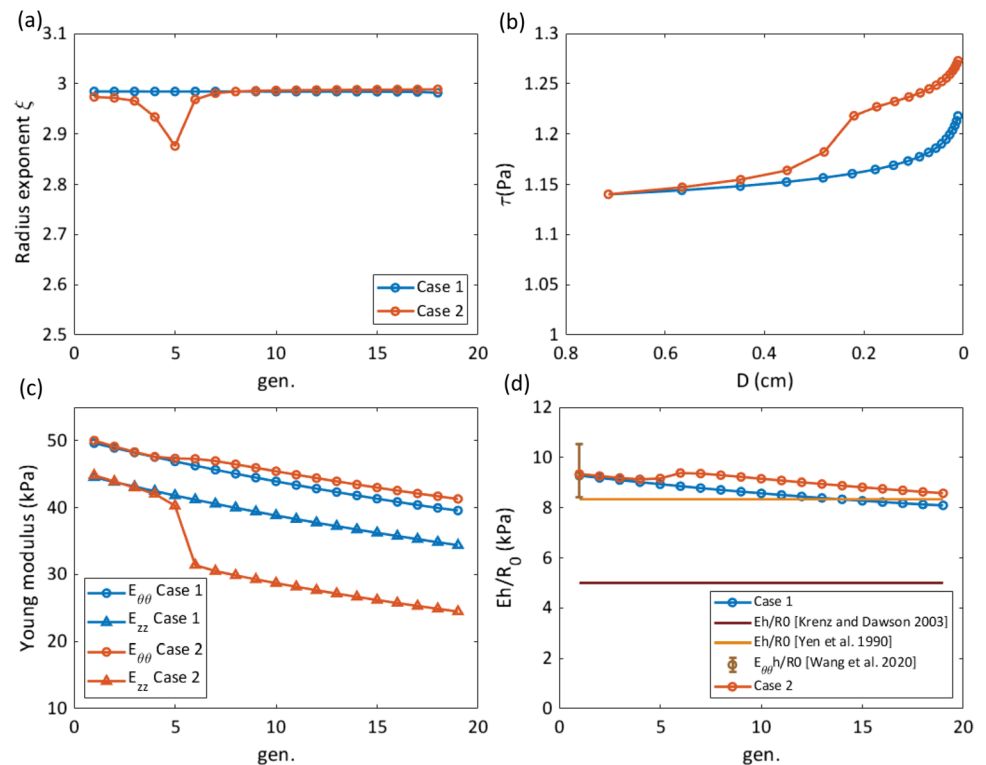
Fig. 7 Symmetric tree—homeostatic optimization results of Case 1 (blue) compared with Case 2 results (red): **a** radius exponent in daughter-to-parent radii relation; **b** homeostatic value of wall shear stress; **c** Young's modulus in circumferential (top) and longitudinal (bottom) directions; **d** circumferential structural stiffness divided by unstressed radius

slow-time blood pressure and flow in the pulmonary arterial tree. We illustrated the utility of our homeostatic optimization framework on examples of symmetric and asymmetric pulmonary trees representing small- to intermediate-size vessels (0.01 to 0.5 cm) of the pulmonary vasculature. The results were presented in terms of the morphometric, structural, and hemodynamics characteristics of the vessels in the tree. Employing our timescale separation framework, the results of the homeostatic optimization were used to obtain the pulsatile hemodynamics using Womersley's analytical solution.

The morphometric results of the optimization have a direct impact on the pulsatile hemodynamics of the pulmonary tree. Hollander et al. (2001) demonstrated that the normal canine pulmonary circulation is characterized by negative wave reflections. The primary factor in producing the negative wave reflections in the pulmonary arterial tree is the rapid increase in the total arterial cross-sectional area over a short distance. Moreover, it has been shown that the negative wave reflection when $a_d/a_p > 1.2$. Our results show an area ratio of $1.2 < a_d/a_p < 1.3$, consistent with pulmonary area ratios reported in various animals (Caro and Saffman 1965; Collins and Maccario 1979), induces a negative wave reflection which can be observed with a sudden drop in pressure after the systolic phase in Fig. 10.

Estimating the arterial stiffness of distal pulmonary vasculature, however, is experimentally challenging. Previous studies employ a distensibility parameter λ, defined as $R/R_0 = 1 + \lambda p$ with pressure p and radius at zero pressure R_0, to characterize the mechanical properties of arterial walls. A meta-analysis by Krenz and Dawson (2003) calculated a constant $\lambda^{KD} = 0.02$ mmHg^{-1} by combining experimental data across multiple species and different sizes of vessels. Moreover, a study on human specimens (Yen et al. 1990) reported $\lambda^{Yen} = 0.012$ mmHg^{-1}, almost constant along the pulmonary arterial tree. For an isotropic incompressible wall, the stiffness measure can be expressed via distensibility parameter as $Eh/R_0 = 3/(4\lambda)$ (Qureshi et al. 2014), where Eh is the structural stiffness (Humphrey et al. 2017). Our homeostatic optimization (Cases 1 and 2) yields an overall mildly decreasing ratio $E_{\theta\theta}h/R_0$ (Figs. 5b, 7d and 8c) that is near the constant value λ^{Yen} and is above λ^{KD}. It must be noted that due to nonlinear mechanics of blood vessels the arterial stiffnesses change with pressure over a cardiac cycle. Therefore, an accurate approximation of the wall stiffness is needed for modeling fluid–structure interactions must be used. Our framework allows incorporating a nonlinear mechanical model (constrained mixture model) of vessels with pulsatile hemodynamics over a whole arterial tree, and calculation of vessels stiffnesses in their in vivo configuration near their respective mean pressure.

We have developed a computational framework in which the complexity of structure and spatial variation has been increased (Case 1, 2, 3) to elucidate their variations for metabolic optimization, hemodynamics, and material properties.

Fig. 8 Asymmetric tree—homeostatic optimization results versus distance (from the root, along the branch pathway), red dots represent optimization results for each vessel, green and blue lines indicate the short and long path, respectively: **a** a random visualization of the tree; **b** terminal steady pressure; **c** ratio of structural stiffness to unstressed radius; **d** homeostatic wall shear stress
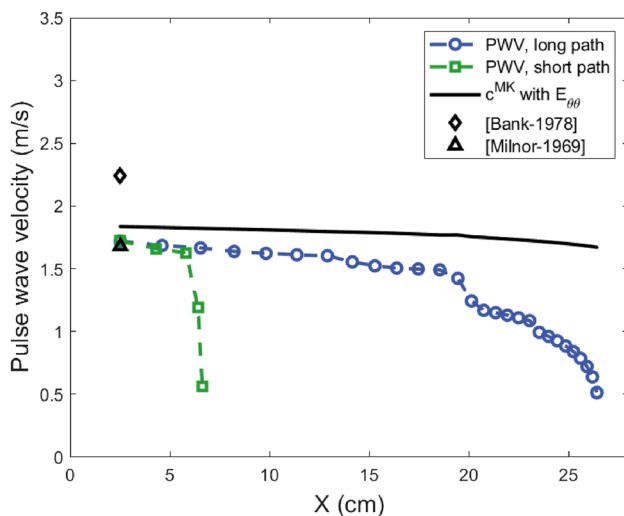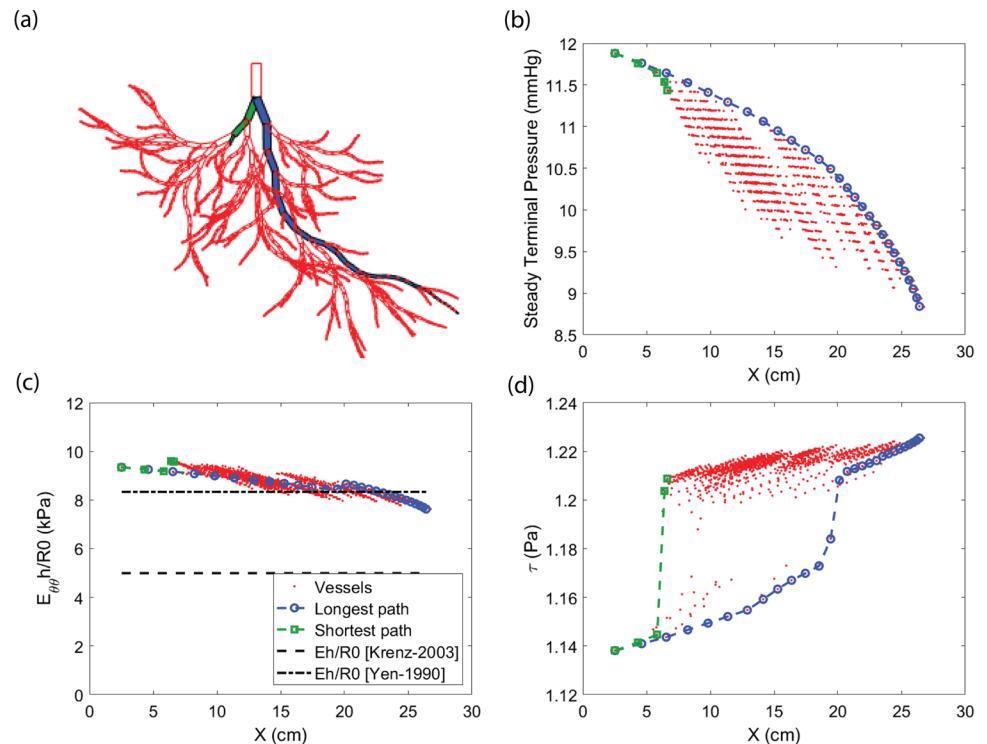

Fig. 9 Asymmetric tree—pulse wave velocity for long and short paths

For instance, introducing a more realistic mass fraction distribution based on available data (in Case 2) has shown to significantly alter the results of the geometry and mechanical properties of the vessels in a pulmonary tree. Across the transition region (Fig. 3) elastin content is reduced and SMCs content is increased which requires a higher metabolic energy for maintenance. Our results show that the energy optimization favors a smaller vessel with a higher percentage of collagen and SMCs to a large vessel with less percentage of collagen and SMCs. This is reflected in a drop

in the radius exponent (Fig. 7a) where a smaller ξ implies smaller parent-to-daughter diameter ratio. In comparison with Case 1, this reduction in vessel sizes across the transition region results in a step-increase of the wall shear stress (Fig. 7b). Moreover, a sudden decrease in the axial Young's modulus of the arteries is caused by replacement of isotropic elastin matrix with SMCs that contribute to stiffness of the wall only in the circumferential direction.

Once the homeostatic state of the pulmonary tree was established, the fast-time framework was used to model the pulsatile hemodynamics. The hemodynamic solution provides the total pressure and flow distribution as well as the pulse wave velocity along the entire tree. Especially, pulse wave velocity is an important hemodynamic factor in PAH (Kopeć et al. 2013) and has been proposed for noninvasive monitoring of pulmonary vasculature (Prins et al. 2016). The predicted pulse wave velocity shows reasonable agreement with available measurements for large pulmonary vessels (Milnor et al. 1969; Banks et al. 1978). Moreover, our results demonstrated a decrease in pulse wave velocity across the generations due to wall stiffness and Womersley's number variabilities. Altogether, the proposed framework will be beneficial for obtaining the impedance outflow boundary conditions essential for coupling distal vasculature with large vessel 3D hemodynamic simulations in the patient-specific models.

The presented framework has several limitations. First, we extended the intrinsic material parameters calibrated for pressure-diameter data for the main pulmonary arteries
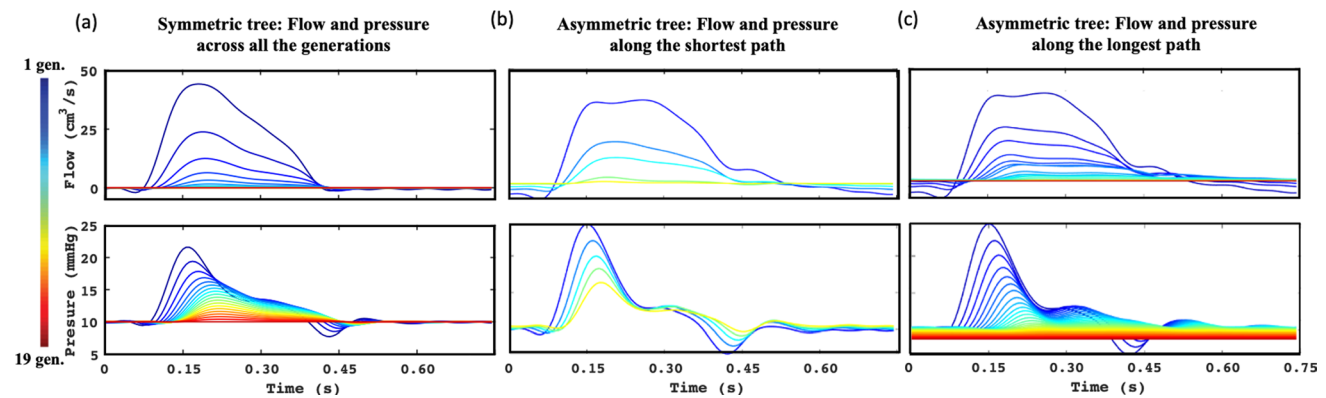
Fig. 10 Symmetric and asymmetric tree—the hemodynamics resulted: Total pressure and flow along all the generations of symmetric tree (column (**a**)), short (column (**a**)) and long (column (**b**)) paths along the asymmetric arterial tree

(Wang et al. 2020) to the whole arterial tree. The underlying assumption was that the mechanical characteristics of constituents remain constant across the tree and only the deposition stretches vary. Nevertheless, more experimental data (pressure-diameter relations and histological analysis) on pulmonary arteries of various sizes can improve the determination of the constrained mixture model parameters and mass fractions. Second, we used a constant blood viscosity, which is justified given the range of vessel sizes. However, for the apparent viscosity changes for vessels < 50 micron, the dependence of apparent viscosity on the vessel size and hematocrit level must be incorporated (Pries and Secomb 2005). Third, another limitation of the current work is that a large set of parameters taken from diverse literature data are used to construct and demonstrate the model. In future, a sensitivity analysis and uncertainty quantification must be done to identify the influence of each parameter on the final output. Fourth, in our Case 3 example, we showed an application of the framework to an asymmetric tree defined by the vessel connectivity from morphometric data (Figs. 8 and 10). However, this reconstruction (visualized in Fig. 8a) represents only a small fraction of the morphometry data in (Huang et al. 1996), with only 1511 vessels. In general, our model can be coupled models with more detailed reconstructions of pulmonary vasculature, such as a volume filling algorithm (Burrowes et al. 2005) or stochastic techniques using morphometry data (e.g., coronary tree reconstruction in (Kaimovitz et al. 2005)). Lastly, in this work we illustrated a one-way coupling example between the slow and fast timescales, where our solution to the pulsatile hemodynamics is merely a post-processing step. However, experimental data have shown that pulsatile factors such as pulse pressure have a direct effect on the structure of vessel walls (Briones et al. 2007). To address this limitation, the presented multiscale framework can be extended to include additional intermediate timescales and include physical regimes that are characterized by bidirectional coupling between governing equations at different timescales.

5 Conclusions

One of the main applications to developing the current model is pulmonary arterial hypertension, which is marked by structural and morphometric changes in the vasculature. The study of evolution of PAH can benefit from computational models that can appropriately describe both the microstructure of the vessels and the overall hemodynamics in the whole arterial network. In this work, we developed a novel method to establish the homeostatic characteristics of an arterial tree. In addition, we formulated a timescale separation framework to develop a model for pulsatile hemodynamics. Our framework can be used to study short- and long-term adaptations in pulmonary arterial networks. Moreover, our model can be coupled with 3D patient-specific hemodynamics models as impedance boundary conditions.

References

Ambrosi D, Ateshian GA, Arruda EM et al (2011) Perspectives on biological growth and remodeling. J Mech Phys Solids 59:863–883. https://doi.org/10.1016/j.jmps.2010.12.011

Avolio AP (1980) Multi-branched model of the human arterial system. Med Biol Eng Comput 18:709–718. https://doi.org/10.1007/BF02441895.

Baek S, Gleason RL, Rajagopal KR, Humphrey JD (2007a) Theory of small on large: potential utility in computations of fluid-solid interactions in arteries. Comput Methods Appl Mech Eng 196:3070–3078. https://doi.org/10.1016/j.cma.2006.06.018

Baek S, Valentín A, Humphrey JD (2007b) Biochemomechanics of cerebral vasospasm and its resolution: II. Constitutive relations and model simulations. Ann Biomed Eng 35:1498. https://doi.org/10.1007/s10439-007-9322-x

Banks J, Booth FV, MacKay EH et al (1978) The physcial properties of human pulmonary arteries and veins. Clin Sci Mol Med 55:477–484

Bernal M, Urban MW, Rosario D et al (2011) Measurement of biaxial mechanical properties of soft tubes and arteries using piezoelectric elements and sonometry. Phys Med Biol 56:3371–3386. https://doi.org/10.1088/0031-9155/56/11/012

Briones AM, Salaices M, Vila E (2007) Mechanisms underlying hypertrophic remodeling and increased stiffness of mesenteric resistance arteries from aged rats. J Gerontol Series A, Biol Sci Med Sci 62(7): 696–706. https://doi.org/10.1093/gerona/62.7.696

Burrowes KS, Hunter PJ, Tawhai MH, Kelly S (2005) Anatomically based finite element models of the human pulmonary arterial and venous trees including supernumerary vessels. J Appl Physiol 99:731–738. https://doi.org/10.1152/japplphysiol.01033.2004

Caro CG, Saffman PG (1965) Extensibility of blood vessels in isolated rabbit lungs. J Physiol 178:193–210. https://doi.org/10.1113/jphysiol.1965.sp007623

Chambers MJ, Colebank MJ, Qureshi MU et al (2020) Structural and hemodynamic properties of murine pulmonary arterial networks under hypoxia-induced pulmonary hypertension. Proc Inst Mech Eng H 234:1312–1329. https://doi.org/10.1177/0954411920944110

Chazova I, Loyd JE, Zhdanov VS et al (1995) Pulmonary artery adventitial changes and venous involvement in primary pulmonary hypertension. Am J Pathol 146:389–397

Clark AR, Tawhai MH (2018) temporal and spatial heterogeneity in pulmonary perfusion: a mathematical model to predict interactions between macro- and micro-vessels in health and disease. ANZIAM J 59:562–580. https://doi.org/10.1017/S1446181118000111

Colebank MJ, Qureshi MU, Rajagopal S et al (2021) A multiscale model of vascular function in chronic thromboembolic pulmonary hypertension. Am J Physiol Heart Circ Physiol 321:H318–H338. https://doi.org/10.1152/ajpheart.00086.2021

Collins R, Maccario JA (1979) Blood flow in the lung. J Biomech 12:373–395. https://doi.org/10.1016/0021-9290(79)90051-4

Elliott FM, Reid L (1965) Some new facts about the pulmonary artery and its branching pattern. Clin Radiol 16:193–198. https://doi.org/10.1016/S0009-9260(65)80042-3

Figueroa CA, Baek S, Taylor CA, Humphrey JD (2009) A computational framework for fluid-solid-growth modeling in cardiovascular simulations. Comput Methods Appl Mech Eng 198:3583–3602. https://doi.org/10.1016/j.cma.2008.09.013

Filonova V, Arthurs CJ, Vignon-Clementel IE, Figueroa CA (2020) Verification of the coupled-momentum method with Womersley's deformable wall analytical solution. Int J Numer Method Biomed Eng 36:e3266. https://doi.org/10.1002/cnm.3266

Guo X, Kassab GS (2004) Distribution of stress and strain along the porcine aorta and coronary arterial tree. Am J Physiol Heart Circ Physiol 286:H2361–H2368. https://doi.org/10.1152/ajpheart.01079.2003

Hislop A, Reid L (1978) Normal structure and dimensions of the pulmonary arteries in the rat. J Anat 125:71–83

Hollander EH, Wang JJ, Dobson GM et al (2001) Negative wave reflections in pulmonary arteries. Am J Physiol Heart Circ Physiol 281:H895-902

Huang W, Yen RT, McLaurine M, Bledsoe G (1996) Morphometry of the human pulmonary vasculature. J Appl Physiol 81:2123–2133. https://doi.org/10.1152/jappl.1996.81.5.2123

Humbert M, Guignabert C, Bonnet S, et al (2019) Pathology and pathobiology of pulmonary hypertension: state of the art and research perspectives. Eur Respir J 53

Humphrey JD, Rajagopal KR (2002) A constrained mixture model for growth and remodeling of soft tissues. Math Models Methods Appl Sci 12:407–430

Humphrey JD, Dufresne ER, Schwartz MA (2014) Mechanotransduction and extracellular matrix homeostasis. Nat Rev Mol Cell Biol 15:802–812. https://doi.org/10.1038/nrm3896

Humphrey JD, Harrison DG, Figueroa CA et al (2017) Central artery stiffness in hypertension and aging: a problem with cause and consequence. Circ Res 118:379–381. https://doi.org/10.1161/CIRCRESAHA.115.307722.Central

Hunter KS, Lee PF, Lanning CJ et al (2008) Pulmonary vascular input impedance is a combined measure of pulmonary vascular resistance and stiffness and predicts clinical outcomes better than pulmonary vascular resistance alone in pediatric patients with pulmonary hypertension. Am Heart J 155:166–174. https://doi.org/10.1016/J.AHJ.2007.08.014

Huo Y, Kassab GS (2007) A hybrid one-dimensional/Womersley model of pulsatile blood flow in the entire coronary arterial tree. Am J Physiol-Heart Circ Physiol 2007 292:6, H2623–H2633. https://doi.org/10.1152/ajpheart.00987.2006

Ionescu C, Oustaloup A, Levron F, et al (2009) A model of the lungs based on fractal geometrical and structural properties. In: IFAC Proceedings Volumes (IFAC-PapersOnline) 15:994–999. https://doi.org/10.3182/20090706-3-FR-2004.0265

Jiang ZL, Kassab GS, Fung YC (1994) Diameter-defined Strahler system and connectivity matrix of the pulmonary arterial tree. J Appl Physiol 76:882–892. https://doi.org/10.1152/jappl.1994.76.2.882

Kaimovitz B, Lanir Y, Kassab GS (2005) Large-scale 3-D geometric reconstruction of the porcine coronary arterial vasculature based on detailed anatomical data. Ann Biomed Eng 33:1517–1535. https://doi.org/10.1007/s10439-005-7544-3

Kamiya A, Bukhari R, Togawa T (1984) Adaptive regulation of wall shear stress optimizing vascular tree function. Bull Math Biol 46:127–137. https://doi.org/10.1016/S0092-8240(84)80038-5

Kopeć G, Moertl D, Jankowski P et al (2013) Pulmonary artery pulse wave velocity in idiopathic pulmonary arterial hypertension. Can J Cardiol 29:683–690. https://doi.org/10.1016/j.cjca.2012.09.019

Krenz GS, Dawson CA (2003) Flow and pressure distributions in vascular networks consisting of distensible vessels. Am J Physiol Heart Circ Physiol 284:H2192–H2203. https://doi.org/10.1152/ajpheart.00762.2002

Li N, Zhang S, Hou J et al (2012) Assessment of pulmonary artery morphology by optical coherence tomography. Heart Lung Circ 21:778–781. https://doi.org/10.1016/J.HLC.2012.07.014

Lindström SB, Satha G, Klarbring A (2015) Extension of Murray's law including nonlinear mechanics of a composite artery wall. Biomech Model Mechanobiol 14:83–91. https://doi.org/10.1007/s10237-014-0590-8

Liu Y, Kassab GS (2007) Vascular metabolic dissipation in Murray's law. Am J Physiol Heart Circ Physiol 292:H1336–H1339. https://doi.org/10.1152/ajpheart.00906.2006

Liu D, Wood NB, Witt N et al (2012) Assessment of energy requirement for the retinal arterial network in normal and hypertensive subjects. J Biomech Eng 134:14501–14507. https://doi.org/10.1115/1.4005529

Mackay EH, Banks J, Sykes B, Lee G (1978) Structural basis for the changing physical properties of human pulmonary vessels with age. Thorax 33:335–344. https://doi.org/10.1136/thx.33.3.335

Marquis AD, Jezek F, Pinsky DJ, Beard DA (2021) Hypoxic pulmonary vasoconstriction as a regulator of alveolar-capillary oxygen flux: a computational model of ventilation-perfusion matching. PLoS Comput Biol 17:e1008861

Milnor WR, Conti CR, Lewis KB, O'Rourke MF (1969) Pulmonary arterial pulse wave velocity and impedance in man. Circ Res 25:637–649

Mittal M, Zhou Y, Ung S et al (2005) A computer reconstruction of the entire coronary arterial tree based on detailed morphometric data. Ann Biomed Eng 33:1015–1026

Murray CD (1926) The physiological principle of minimum work applied to the angle of branching of arteries. Proc Natl Acad Sci 12:835–841

Nichols WW, O'Rourke MF, Vlachopoulos C (2011) McDonald's blood flow in arteries: theoretical, experimental and clinical principles, Sixth. Hodder Arnold

Olufsen MS, Peskin CS, Kim WY et al (2000) Numerical simulation and experimental validation of blood flow in arteries with structured-tree outflow conditions. Ann Biomed Eng 28:1281–1299. https://doi.org/10.1114/1.1326031

Olufsen MS, Hill NA, Vaughan GDA et al (2012) Rarefaction and blood pressure in systemic and pulmonary arteries. J Fluid Mech 705:280–305. https://doi.org/10.1017/jfm.2012.220

Paul R (1980) Chemical energetics of vascular smooth muscle. Compr Physiol 2007:1–16. https://doi.org/10.1002/cphy.cp020209

Pries AR, Secomb TW (2005) Microvascular blood viscosity in vivo and the endothelial surface layer. Am J Physiol Heart Circ Physiol 289:H2657–H2664. https://doi.org/10.1152/ajpheart.00297.2005

Pries AR, Secomb TW, Gaehtgens P (1995) Design principles of vascular beds. Circ Res 77:1017–1023. https://doi.org/10.1161/01.RES.77.5.1017

Pries AR, Reglin B, Secomb TW (2005) Remodeling of blood vessels. Hypertension 46:725–731. https://doi.org/10.1161/01.HYP.0000184428.16429.be

Prins KW, Weir EK, Archer SL et al (2016) Pulmonary pulse wave transit time is associated with right ventricular–pulmonary artery coupling in pulmonary arterial hypertension. Pulm Circ 6:576–585. https://doi.org/10.1086/688879

Qureshi MU, Vaughan GDA, Sainsbury C et al (2014) Numerical simulation of blood flow and pressure drop in the pulmonary arterial and venous circulation. Biomech Model Mechanobiol 13:1137–1154. https://doi.org/10.1007/s10237-014-0563-y

Rol N, Timmer EM, Faes TJC et al (2017) Vascular narrowing in pulmonary arterial hypertension is heterogeneous: rethinking resistance. Physiol Rep 5:e13159. https://doi.org/10.14814/phy2.13159

Seyedsalehi S, Zhang L, Choi J, Baek S (2015) Prior distributions of material parameters for bayesian calibration of growth and remodeling computational model of abdominal aortic wall. J Biomech Eng 10(1115/1):4031116

Stacher E, Graham BB, Hunt JM et al (2012) Modern age pathology of pulmonary arterial hypertension. Am J Respir Crit Care Med 186(3):261-72. https://doi.org/10.1164/RCCM.201201-0164OC

Taber LA (1998) An optimization principle for vascular radius including the effects of smooth muscle tone. Biophys J 74:109–114

Tamaddon H, Behnia M, Behnia M, Kritharides L (2016) A new approach to blood flow simulation in vascular networks. Comput Methods Biomech Biomed Eng 19:673–685. https://doi.org/10.1080/10255842.2015.1058926

Taylor MG (1957) An approach to an analysis of the arterial pulse wave I. Oscillations in an attenuating line. Phys Med Biol 1:258–269

Townsley M (2012) Structure and composition of pulmonary arteries, capillaries, and veins. Compr Physiol 2:675–709. https://doi.org/10.1002/cphy.c100081

Truong U, Fonseca B, Dunning J et al (2013) Wall shear stress measured by phase contrast cardiovascular magnetic resonance in children and adolescents with pulmonary arterial hypertension. J Cardiovasc Magn Reson 15:1–9. https://doi.org/10.1186/1532-429X-15-81

Tuder RM (2016) Pulmonary vascular remodeling in pulmonary hypertension. Cell Tissue Res 3(367):643–649. https://doi.org/10.1007/S00441-016-2539-Y

van de Vosse FN, Stergiopulos N (2011) Pulse wave propagation in the arterial tree. Annu Rev Fluid Mech 43:467–499. https://doi.org/10.1146/annurev-fluid-122109-160730

Wang Z, Chesler NC (2011) Pulmonary vascular wall stiffness: an important contributor to the increased right ventricular afterload with pulmonary hypertension. Pulm Circ 1:212–223. https://doi.org/10.4103/2045-8932.83453

Wang Y, Gharahi H, Grobbel MR et al (2020) Potential damage in pulmonary arterial hypertension: an experimental study of pressure-induced damage of pulmonary artery. J Biomed Mater Res Part A. https://doi.org/10.1002/jbm.a.37042

Womersley JR (1957) Oscillatory flow in arteries : the constrained elastic tube as a model of arterial flow and pulse transmission. Phys Med Biol 2:178–187

Yen RT, Tai D, Rong Z, Zhang B (1990) Elasticity of pulmonary blood vessels in human lungs. In: Epstein MAF, Ligas JR (eds) Respiratory biomechanics: engineering analysis of structure and function. Springer-Verlag, New York

Zambrano BA, McLean NA, Zhao X et al (2018) Image-based computational assessment of vascular wall mechanics and hemodynamics in pulmonary arterial hypertension patients. J Biomech 68:84–92. https://doi.org/10.1016/j.jbiomech.2017.12.022